Nano Research

ISSN 1998-0124 CN 11-5974/O4
https://doi.org/10.26599/NR.2026.94909246

Research Article

Molecularly deposited titanium–dienediol hybrid photoresists for high-resolution electron-beam and EUV lithography

Yutao Xu[1,3], Xingkun Wang[1], Zhixing Ren[2], Jianan Xie[2,3], Miao Meng[1], Fanghao Xu[1], Zhaolei Liang[1], Muhan Tang[1], Yazhuo Xie[1], Zhenjiang Li[3](✉), Jun Zhao[3](✉), Renzhong Tai[3](✉), Feng Luo[1,2,3](✉)

[1] Tianjin Key Lab for Rare Earth Materials and Applications, Center for Rare Earth and Inorganic Functional Materials, Smart Sensor Interdisciplinary Science Center, School of Materials Science and Engineering, Nankai University, Tianjin 300350, China

[2] College of Electronic Information and Optical Engineering, Nankai University, Tianjin 300350, China

[3] Shanghai Synchrotron Radiation Facility, Shanghai Institute of Applied Physics, Chinese Academy of Sciences, Shanghai 201204, China

Nano Res., **Just Accepted Manuscript** • https://doi.org/10.26599/NR.2026.94909246

https://www.sciopen.com/journal/1998-0124 on Oct. 7, 2026

© The Authors(s)

Just Accepted

This is a "Just Accepted" manuscript, which has been examined by the peer-review process and has been accepted for publication. A "Just Accepted" manuscript is published online shortly after its acceptance,which is prior to technical editing and formatting and author proofing. Tsinghua University Press (TUP) provides "Just Accepted" as an optional and free service which allows authors to make their results available to the research community as soon as possible after acceptance. After a manuscript has been technically edited and formatted, and the page proofs have been corrected, it will be removed from the "Just Accepted" web site and published officially with volume and article number (e.g., *Nano Research*, **2025**, *18*, 94906990). Please note that technical editing may introduce minor changes to the manuscript text and/or graphics which may affect the content, and all legal disclaimers that apply to the journal pertain. In no event shall TUP be held responsible for errors or consequences arising from the use of any information contained in these "Just Accepted" manuscripts. To cite this anuscript please use its Digital Object Identifier (DOI®),which is identical for all formats of publication.

Just Accepted

Research Article

Molecularly deposited titanium–dienediol hybrid photoresists for high-resolution electron-beam and EUV lithography

Yutao Xu[1,3], Xingkun Wang[1], Zhixing Ren[2], Jianan Xie[2,3], Miao Meng[1], Fanghao Xu[1], Zhaolei Liang[1], Muhan Tang[1], Yazhuo Xie[1], Zhenjiang Li[3,*], Jun Zhao[3,*], Renzhong Tai[3,*], and Feng Luo[1,2,3,*]

[1] Tianjin Key Lab for Rare Earth Materials and Applications, Center for Rare Earth and Inorganic Functional Materials, Smart Sensor Interdisciplinary Science Center, School of Materials Science and Engineering, Nankai University, Tianjin 300350, China

[2] College of Electronic Information and Optical Engineering, Nankai University, Tianjin 300350, China

[3] Shanghai Synchrotron Radiation Facility, Shanghai Institute of Applied Physics, Chinese Academy of Sciences, Shanghai 201204, China

Received: 1 July 2026; **Revised:** 3 October 2026; **Accepted:** 7 October 2026

* Address correspondence to Zhenjiang Li, lizhenjiang@sari.ac.cn; Jun Zhao, zhaoj@sari.ac.cn; Renzhong Tai, tairenzhong@sinap.ac.cn; Feng Luo, feng.luo@nankai.edu.cn

Cite this article: *Nano Research*, 2026, 19, 94909246 https://doi.org/10.26599/NR.2026.94909246

Just Accepted

Abstract

Vapor-phase metal–organic photoresists are promising for nanoscale lithography because they combine solvent-minimized processing, conformal ultrathin-film formation, and inorganic-network-enabled pattern stability. However, the molecular origin of their radiation-induced solubility switching remains insufficiently resolved. Here, we report a molecular-layer-deposited titanium–dienediol hybrid photoresist, Ti–DVG, prepared from a titanium precursor and 1,5-hexadiene-3,4-diol. The hydroxyl groups enable sequential molecular layer deposition, while the terminal alkenes introduce unsaturated carbon environments that undergo irradiation-induced transformation within the Ti–organic network. Ti–DVG exhibits nearly linear growth at ca. 0.10 nm cycle $^{-1}$, smooth continuous morphology, and a negative-tone response after electron-beam exposure and development. Electron-beam lithography produces continuous 25 nm line/space

patterns with line-edge roughness values of 2.347–2.959 nm, while low-contrast limiting features down to approximately 5.2 nm are observed under size-specific exposure conditions, including the use of thinner films for the sub-10 nm tests. EUV interference lithography further resolves dense patterns with half-pitches down to 15–18 nm. Complementary FTIR, background-subtracted outgassing, XPS, repeated-scan XPS, and Raman analyses collectively support ligand transformation, volatile-species evolution, oxygen-environment redistribution, and formation of Ti–O-rich local structures. This work establishes a mechanistically traceable design strategy for vapor-phase hybrid photoresists.

Keywords: molecular layer deposition; vapor-phase photoresist; titanium hybrid network; electron-beam lithography; EUV lithography; nanoscale patterning

Introduction

Continued dimensional scaling in semiconductor manufacturing places increasingly stringent requirements on photoresist materials. As the target feature size approaches the few-tens-of-nanometers regime, resist films must simultaneously provide high radiation sensitivity, low line-edge roughness, sufficient etch resistance, and mechanical stability against pattern collapse [1–3]. Conventional spin-coated organic photoresists have enabled decades of lithographic progress, but their solution-based film formation, relatively low EUV absorption, stochastic acid-diffusion chemistry, and capillary-force-induced collapse become increasingly limiting for high-resolution electron-beam lithography and extreme ultraviolet (EUV) lithography [1, 2, 4–6]. Metal-containing photoresists have been developed to address several of these limitations [7]. Incorporation of high-atomic-number elements can increase EUV absorption and enhance secondary-electron generation, while inorganic or hybrid networks can improve plasma etch resistance relative to purely organic polymer resists [5, 8–10]. Representative material platforms include metal oxo clusters, organometallic small molecules, nanoparticles, and inorganic–organic hybrid films [9–13]. Recent high-absorption and inorganic-framework resist platforms further highlight the importance of integrating strong EUV absorbers, efficient radiation-responsive bonds, and molecularly homogeneous architectures to balance sensitivity, resolution, and pattern stability [14, 15]. However, many metal-containing resists are still processed by spin coating and wet development, which introduces thickness nonuniformity, solvent compatibility constraints,

Just Accepted

and capillary stresses during development. These issues are particularly problematic for ultrathin films and high-aspect-ratio nanoscale patterns.

Dry photoresists based on vapor-phase film formation provide a fundamentally different route to resist design [16, 17]. By replacing spin coating with chemical vapor deposition, atomic layer deposition, or molecular layer deposition, resist synthesis and film formation can be integrated into a surface-controlled process. Molecular layer deposition (MLD) is especially attractive because it enables the construction of inorganic–organic hybrid networks with Å-scale thickness control, conformal coverage, and tunable molecular structure [16, 18–20]. Recent studies on MLD-derived Hf-, Al-, and Zn-containing hybrid films have demonstrated the feasibility of using vapor-deposited metal–organic materials as electron-beam or EUV resists [17, 19, 20]. Nevertheless, many reported dry-resist systems are evaluated mainly from the perspective of lithographic performance, while the molecular connection between precursor design, radiation-induced chemical conversion, and nanoscale pattern formation remains insufficiently clarified.

Titanium-based hybrid networks offer an opportunity to address this gap. Ti–O frameworks are chemically robust and can form inorganic-rich structures after radiation-induced ligand transformation. At the same time, organic co-reactants containing unsaturated bonds can introduce irradiation-transformable carbon environments that may participate in radical reactions, fragmentation, or network rearrangement [12, 21]. We therefore hypothesized that a Ti-based metal–organic film constructed from a dienediol ligand could serve not only as a dry photoresist but also as a model system for understanding how vapor-deposited hybrid networks generate solubility contrast under high-energy irradiation.

Here, we report a molecular-layer-deposited Ti–DVG hybrid photoresist as a vapor-phase nanolithographic material. The material is prepared from a titanium precursor and 1,5-hexadiene-3,4-diol, in which the hydroxyl groups support sequential MLD growth and the terminal alkene groups introduce unsaturated carbon environments that undergo irradiation-induced transformation. This molecular design enables the Ti–organic network to integrate three functions that are central to high-resolution nanolithography: controlled ultrathin-film formation, exposure-induced solubility switching, and inorganic-enriched pattern stabilization. Ti–DVG shows nearly linear MLD growth, smooth film morphology, and negative-tone patterning behavior. Electron-beam and EUV interference lithography demonstrate nanoscale pattern

Just Accepted

formation, including 25 nm line/space EBL patterns, limiting features down to approximately 5 nm, and EUV half-pitches down to 15–18 nm. By combining FTIR, outgassing analysis, XPS, repeated-scan XPS, and Raman spectroscopy, we obtain complementary evidence that the lithographic response involves exposure-induced ligand transformation and conversion of the Ti–organic network toward a more Ti–O-rich local structure. These results establish Ti–DVG as a mechanistically traceable vapor-phase photoresist and provide a molecular design strategy for dry metal–organic nanolithographic materials.

Results and Discussion

Molecular Design, MLD Growth, and Dose Response of Ti–DVG

Ti–DVG was designed as a molecularly deposited titanium–dienediol hybrid photoresist that integrates vapor-phase film growth with exposure-responsive organic chemistry [16, 18, 19]. As shown in Figure 1a,b, alternating reactions between the titanium precursor and 1,5-hexadiene-3,4-diol generate a Ti–O–C hybrid network containing dienediol-derived unsaturated organic units. The hydroxyl groups of the dienediol enable sequential MLD growth, whereas the terminal alkene groups introduce unsaturated carbon environments that undergo transformation during subsequent irradiation [12, 18].

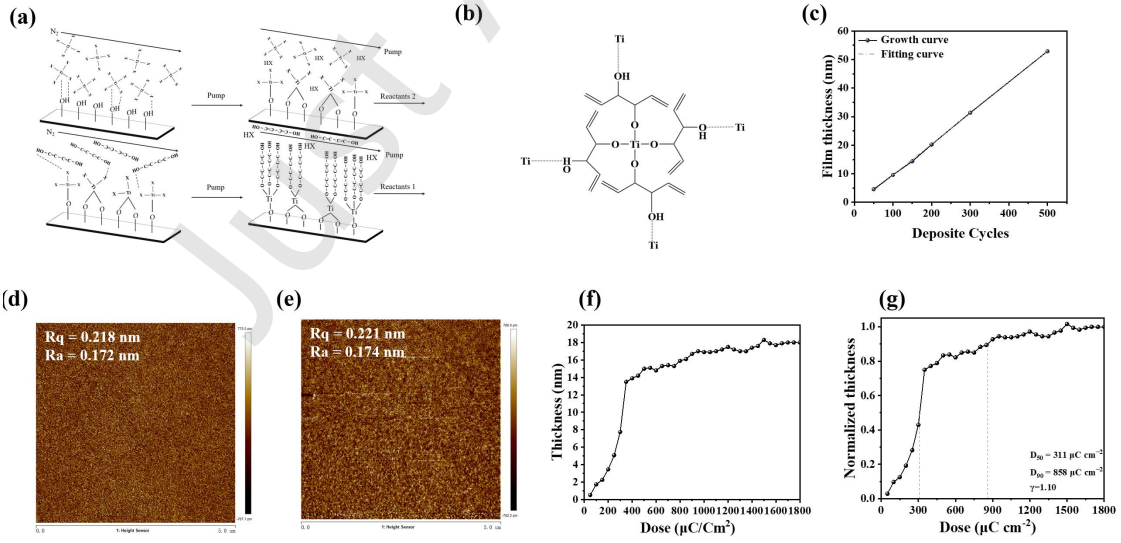


Figure 1. Molecular design, MLD growth, surface morphology, and dose response of the Ti–DVG hybrid photoresist. (a) Schematic illustration of the MLD process for Ti–DVG. (b) Proposed Ti–DVG hybrid network containing Ti–O–C linkages and dienediol-derived unsaturated units. (c) Film thickness as a function of MLD cycle number. (d,e) AFM height images of as-deposited Ti–DVG films. (f) Absolute remaining film thickness after

Just Accepted

electron-beam exposure and development. (g) Normalized remaining thickness, T/T_0, as a function of exposure dose. The extracted D_{10}, D_{50}, D_{90}, and contrast value are 105.9 μC cm^{-2}, 310.9 μC cm^{-2}, 858.3 μC cm^{-2}, and 1.10, respectively.

The Ti–DVG film shows nearly linear thickness growth with MLD cycle number, reaching approximately 52 nm after 500 cycles and giving a growth rate close to 0.10 nm cycle^{-1} (Figure 1c). AFM images confirm that the as-deposited films are smooth and continuous (Figure 1d,e), which is important for evaluating nanoscale patterning without significant roughness contributions from the initial film surface. Additional AFM images recorded over different scan regions further confirm the sub-nanometer surface roughness of the as-deposited Ti–DVG films (Figure S2). After electron-beam exposure and development, Ti–DVG exhibits a clear negative-tone dose response (Figure 1f,g), indicating exposure-induced insolubilization of the hybrid network [17, 19, 20]. The extracted D_{10}, D_{50}, D_{90}, and contrast values are 105.9 μC cm^{-2}, 310.9 μC cm^{-2}, 858.3 μC cm^{-2}, and 1.10, respectively. The measurable solubility transition provides a practical processing window for evaluating nanoscale pattern formation. The combination of controllable MLD growth, smooth initial morphology, and negative-tone solubility switching makes Ti–DVG suitable for subsequent EBL and EUV lithographic tests.

The contrast value of 1.10 reflects a gradual solubility transition and should be regarded as moderate rather than exceptional relative to reported MLD-derived metal-containing photoresists. This behavior is consistent with a non-chemically amplified hybrid film in which ligand transformation and Ti–O-network rearrangement proceed progressively over a distributed dose range. Within the sensitivity–resolution–roughness trade-off, the significance of Ti–DVG lies in the integration of surface-controlled Ti–dienediol film formation, electron-beam and EUV patternability, and complementary characterization of the coupled organic–inorganic conversion process, rather than in an unusually sharp dose response [17, 19, 20].

Electron-Beam Nanolithography and Pattern-Transfer Potential

The nanoscale patternability of Ti–DVG was first evaluated by EBL, a standard high-resolution platform for assessing emerging molecular, inorganic, and hybrid resist materials [19, 20, 22]. Figure 2 summarizes representative line/space patterns, including quantitative 25 nm features and limiting-resolution patterns.

Just Accepted

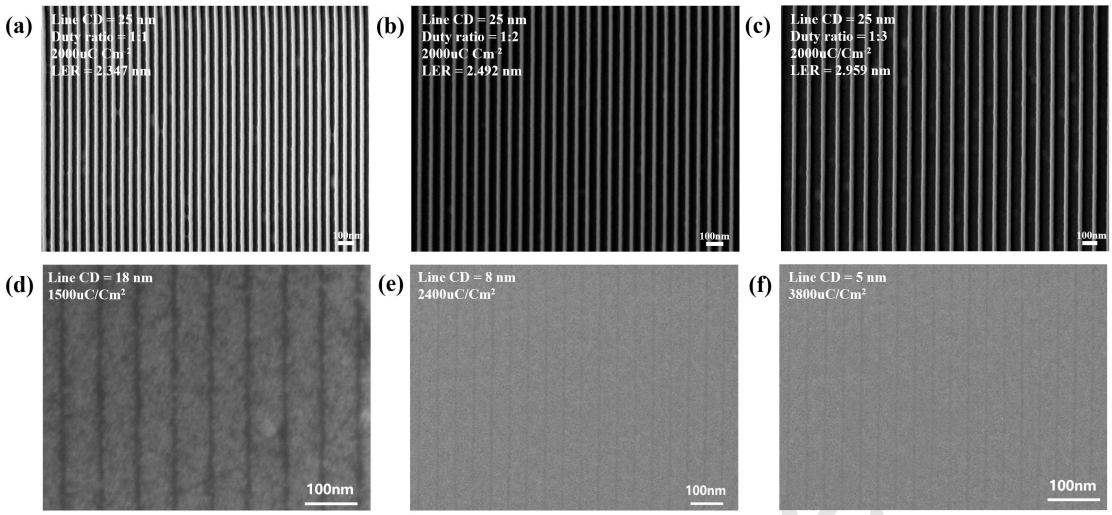


Figure 2. Electron-beam lithographic patterning of Ti–DVG. (a–c) Quantitative 25 nm line/space patterns with different duty ratios, showing LER values of 2.347, 2.492, and 2.959 nm, respectively. (d–f) Limiting-feature patterns with measured critical dimensions of 18, 8, and 5 nm, respectively, obtained under size-specific exposure conditions. The 8 and 5 nm patterns in (e,f) were obtained using nominally 10-nm-thick films, whereas the 18 nm pattern in (d) was obtained using an approximately 30-nm-thick film. The smaller retained resist volume in the sub-10 nm tests likely contributes to the reduced SEM material contrast and prevents reliable LER extraction; these panels are therefore presented as limiting-feature demonstrations rather than quantitative roughness benchmarks.

At an exposure dose of 2000 μC cm $^{-2}$, Ti–DVG produced continuous 25 nm line/space patterns with duty ratios of 1:1, 1:2, and 1:3, corresponding to LER values of 2.347, 2.492, and 2.959 nm, respectively (Figure 2a–c). This demonstrates that the MLD-derived Ti–DVG film can translate its negative-tone response into well-defined nanoscale line/space features across different pattern densities. Smaller features with measured critical dimensions of 18, 8, and 5 nm were observed under size-specific exposure conditions (Figure 2d–f). The 8 and 5 nm features were obtained using nominally 10-nm-thick films, whereas the 18 nm feature was obtained using an approximately 30-nm-thick film. The thinner-film condition was used for the sub-10 nm tests to help limit linewidth broadening and improve pattern stability. The smaller retained resist volume in these tests likely contributes to the reduced SEM material contrast. These ultrafine patterns are therefore presented as limiting-feature demonstrations rather than as quantitative LER measurements or an optimized process window. Additional EBL patterns with different feature sizes and duty ratios are provided in Figure S3, and enlarged SEM images of the ultrafine features are provided in Figure S4.

In addition to direct pattern formation, Ti–DVG shows preliminary pattern-transfer potential. After development, the patterned Ti–DVG layer remained effective as an etch-resistant mask

Just Accepted

under the tested plasma conditions (Figure S5), demonstrating that the exposure-induced Ti–O-rich network can support nanoscale pattern transfer. Although further process optimization is required, this result extends the relevance of Ti–DVG beyond imaging-only demonstrations [20, 23].

EUV Interference Lithography of Ti–DVG

EUV interference lithography was used to further evaluate the photon-based high-resolution patternability of Ti–DVG, using a synchrotron-based EUV-IL approach for advanced photoresist evaluation [1, 5, 24]. Representative dense line/space patterns with half-pitches from 50 to 15 nm are shown in Figure 3. The reported exposure doses were corrected by the corresponding grating efficiency.

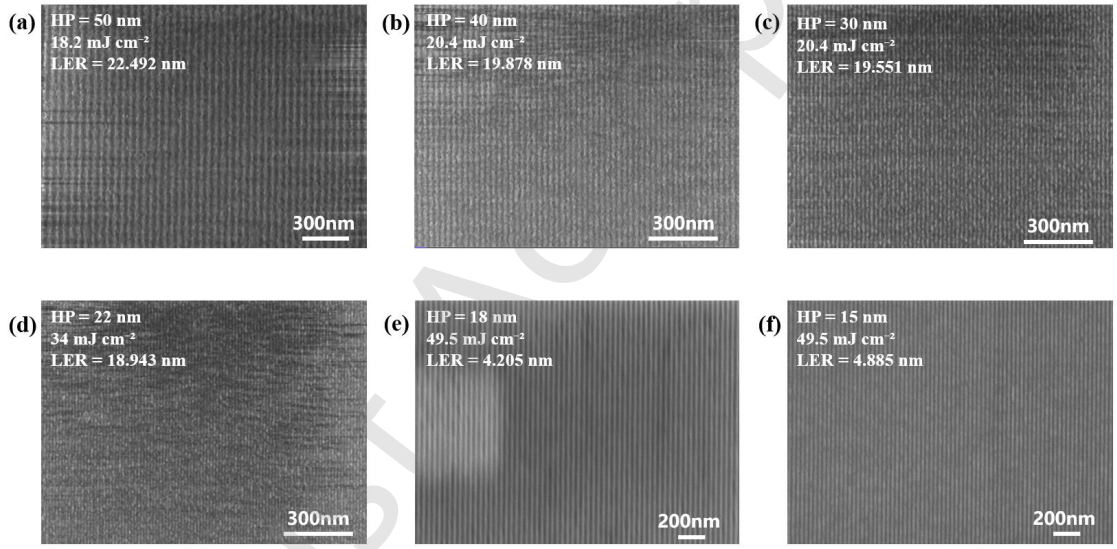


Figure 3. EUV interference lithographic patterning of Ti–DVG. (a–d) Representative line/space patterns with half-pitches of 50, 40, 30, and 22 nm obtained at the Hefei light source. (e,f) Optimized sub-20 nm half-pitch patterns with HP 18 nm and HP 15 nm obtained at the SSRF. Because the patterns were obtained in different exposure sessions and sample histories, the LER values are used to evaluate representative pattern quality rather than to establish a direct half-pitch-dependent trend.

Ti–DVG generated periodic EUV line/space patterns over a broad half-pitch range from 50 to 15 nm (Figure 3). At the Hefei light source, HP 50, 40, and 30 nm patterns were obtained at corrected doses of 18.2–20.4 mJ cm $^{-2}$, indicating efficient EUV-induced solubility switching of the Ti-based vapor-phase photoresist. Under optimized conditions at SSRF, clearer sub-20 nm patterns were obtained at HP 18 and 15 nm, with LER values of 4.205 and 4.885 nm,

Just Accepted

respectively [9, 23, 24]. Because the HP 50–22 nm and HP 18–15 nm patterns were obtained in different exposure sessions and with different sample histories, these data are used to demonstrate broad EUV patternability rather than to establish a direct half-pitch-dependent dose or LER trend. The comparison also suggests that pre-exposure storage and ambient exposure should be carefully controlled for vapor-deposited metal–organic photoresists [9, 25].

FTIR and Outgassing Evidence for Radiation-Induced Ligand Transformation

Compared with conventional polymer photoresists, the exposure chemistry of vapor-phase-deposited dry photoresists is more difficult to elucidate. Most dry metal–organic resist films are amorphous or weakly ordered, so their exposure-induced conversion cannot be tracked through straightforward lattice or crystallographic changes. In addition, the ultrathin-film geometry that benefits nanoscale lithography also limits the amount of material available for characterization. Many bulk-sensitive techniques are therefore difficult to apply directly because the signal from an ultrathin resist layer is weak and can be influenced by the substrate, gas-phase species, or instrumental background. Therefore, the mechanism of dry-resist conversion must be constructed from complementary thin-film-compatible measurements rather than from a single definitive structural probe [10–12].

To obtain a chemically meaningful picture of Ti–DVG conversion, FTIR spectroscopy and outgassing analysis were used to probe exposure-induced changes in organic bonding environments and volatile-fragment release [10–12, 26]. For both measurements, background data were acquired under the same instrumental conditions before sample-data collection and were subtracted from the displayed spectra. The FTIR spectra of the unexposed and exposed films were collected using identical acquisition parameters. Similarly, the outgassing spectrum represents the differential signal obtained after subtraction of the pre-exposure background. The following discussion therefore focuses on exposure-correlated changes rather than on static atmospheric or chamber-background contributions. The results are summarized in Figure 4.

Just Accepted

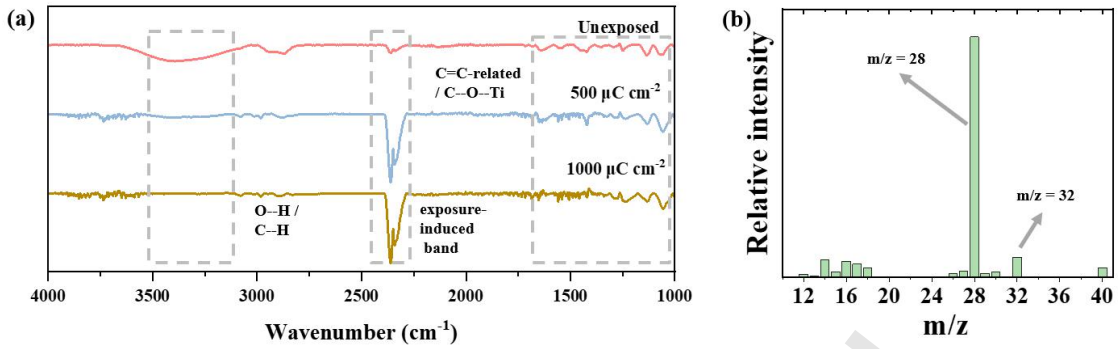


Figure 4. FTIR and outgassing evidence for exposure-induced ligand transformation in Ti–DVG. (a) Background-corrected FTIR spectra of Ti–DVG before and after electron-beam exposure. The feature in the 2300–2400 cm $^{-1}$ region is weak in the unexposed film but becomes more pronounced after exposure, together with changes in the C=C- and C–O–Ti-related regions. (b) Background-subtracted outgassing spectrum collected during irradiation, showing several exposure-induced mass channels, including a prominent differential signal at $m/z = 28$. Because isobaric species cannot be uniquely distinguished by the present mass-spectrometric measurement, no unique molecular assignment is made for the $m/z = 28$ channel. Collectively, these results support irradiation-induced ligand transformation and volatile-species evolution.

The background-corrected FTIR spectra show exposure-correlated changes in the Ti–DVG film. In particular, the feature in the 2300–2400 cm $^{-1}$ region is weak in the unexposed film but becomes progressively more pronounced after exposure at 500 and 1000 μC cm $^{-2}$. Because the background was acquired and subtracted using the same measurement procedure, a temporally invariant atmospheric CO $_2$ contribution should be largely cancelled. Moreover, a static atmospheric background alone cannot readily account for the exposure-dependent evolution relative to the unexposed control. We therefore associate this feature with an irradiation-correlated species rather than with an unchanged atmospheric background. Nevertheless, because this spectral window overlaps with CO $_2$-related absorption and FTIR alone cannot distinguish a film-bound product from an irradiation-generated gaseous species, no unique molecular assignment is made. Accordingly, this band is described only as an exposure-correlated spectral feature and is used as supporting evidence for ligand transformation rather than as standalone proof of a specific reaction product.

Background-subtracted outgassing analysis provides complementary evidence for irradiation-induced volatile-species evolution. A background mass spectrum was acquired before exposure and subtracted from the spectrum collected during irradiation. In addition, no N $_2$ was intentionally introduced into the exposure chamber. Consequently, a static residual N $_2$ background is unlikely to be the dominant origin of the exposure-induced differential signal at

Just Accepted

$m/z = 28$. Nevertheless, because species with the same nominal mass cannot be uniquely distinguished at the available mass resolution, the molecular identity of this channel cannot be determined unambiguously. We therefore describe it only as an exposure-induced $m/z = 28$ channel. The outgassing results demonstrate irradiation-correlated volatile evolution, while no unique molecular assignment is made for this channel [10, 12, 26, 27]. Together with the FTIR and XPS changes, these results support ligand cleavage or rearrangement as part of the exposure-induced conversion of Ti–DVG.

XPS Evidence for Carbon Consumption and Oxygen-Environment Redistribution

The FTIR and outgassing results provide qualitative evidence that exposure induces ligand transformation and volatile-species evolution. To further examine whether this process is accompanied by changes in the chemical bonding environments of Ti–DVG, XPS spectra were collected before and after exposure. Because XPS peak fitting can be sensitive to background selection, peak-position constraints, and line-shape parameters, the fitted component areas are interpreted mainly as relative trends rather than absolute chemical-state quantification [28]. The XPS results are summarized in Figure 5. To further validate these exposure-induced trends while minimizing ambient and transfer effects, a repeated-scan XPS experiment was performed on the same Ti–DVG region under vacuum (Figure S6).

Just Accepted

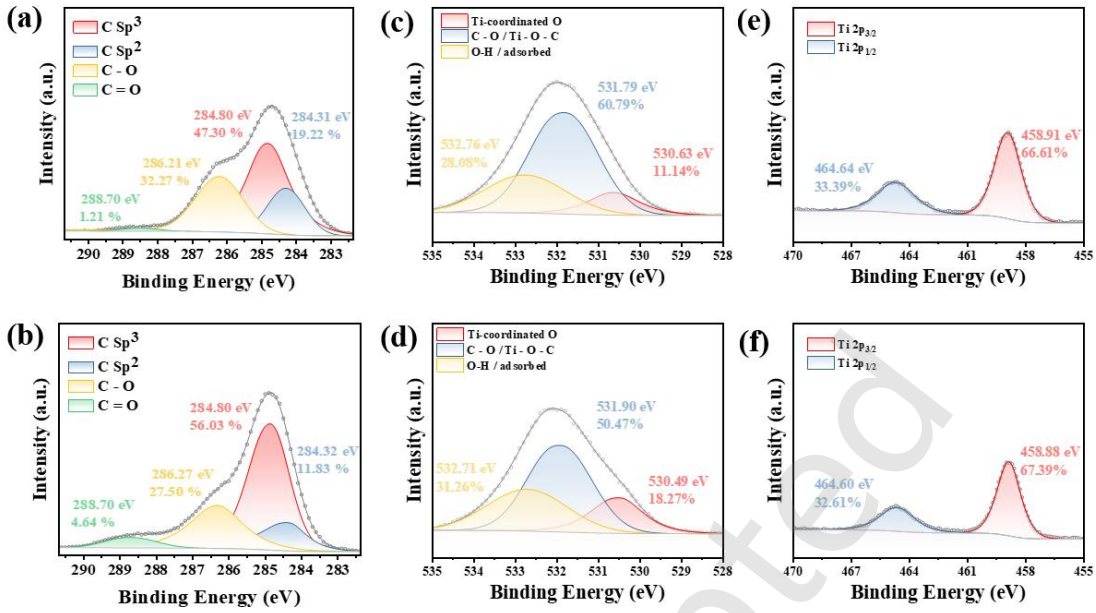


Figure 5. XPS evidence for exposure-induced chemical evolution of Ti–DVG. (a,b) C 1s spectra before and after exposure, respectively. (c,d) O 1s spectra before and after exposure, respectively. (e,f) Ti 2p spectra before and after exposure, respectively. The C 1s spectra show decreased sp^2 C/C=C and an increased high-binding-energy oxidized-carbon contribution after exposure, while the O 1s spectra reveal an increased Ti-coordinated O contribution and a decreased C–O/Ti–O–C-related contribution. The Ti 2p spectra remain dominated by Ti(IV)-like oxygen-coordinated Ti species.

As shown in Figure 5a,b, the C 1s spectra show pronounced changes after exposure. Using identical fitting constraints, the sp^2 C/C=C component decreases from 19.22% to 11.83%, while the sp^3 C/C–C component increases from 47.30% to 56.03%. The C–O/C–O–Ti component also decreases from 32.27% to 27.50%, suggesting partial cleavage or rearrangement of Ti–organic linkages. In addition, the relative fitted area of the high-binding-energy oxidized-carbon component near 288.7 eV increases from 1.21% to 4.64% after exposure. Because several oxidized-carbon environments may contribute within this binding-energy region, this component is not assigned to a unique molecular species. These changes suggest preferential consumption or transformation of the dienediol-derived unsaturated carbon environments during irradiation [10–12]. The increase in the relative high-binding-energy carbon contribution is not inconsistent with the outgassing results because the two measurements probe different material fractions. Outgassing analysis detects volatile species released from the film during irradiation, whereas XPS characterizes the solid material remaining after exposure. Irradiation can therefore cause the loss of part of the organic ligand as volatile carbon-containing species while leaving a smaller oxidized-carbon fraction in the residual film. Moreover, the fitted C 1s component percentages

Just Accepted

are normalized to the remaining C 1s signal and should not be interpreted as absolute carbon concentrations.

The O 1s spectra provide complementary evidence for redistribution of oxygen-containing bonding environments. As shown in Figure 5c,d, the Ti-coordinated O component increases from 11.14% at 530.63 eV to 18.27% at 530.49 eV after exposure. In contrast, the dominant C–O/Ti–O–C-related component decreases from 60.79% at 531.79 eV to 50.47% at 531.90 eV, while the O–H/adsorbed-O-related component slightly increases from 28.08% at 532.76 eV to 31.26% at 532.71 eV. Because the O 1s region contains strongly overlapping contributions from Ti–O, Ti–O–C, C–O, hydroxyl, and adsorbed oxygen species, these fitted components are used to describe relative oxygen-environment redistribution rather than to claim crystalline TiO_2 formation or to independently quantify C=O oxygen species. Overall, the increase in Ti-coordinated oxygen together with the decrease in the C–O/Ti–O–C-related contribution supports exposure-induced rearrangement of the Ti–organic bonding environment toward a more Ti–O-rich local network.

The Ti 2p spectra remain largely unchanged after exposure (Figure 5e,f). The Ti $2p_{3/2}$ peak is located at approximately 458.9 eV, with a spin–orbit splitting of about 5.7 eV, indicating that Ti remains predominantly in a Ti(IV)-like oxygen-coordinated environment. The weak response of the Ti 2p region is reasonable because the exposure-induced conversion mainly involves ligand consumption, C–O/Ti–O–C rearrangement, and redistribution of oxygen-containing bonding environments, rather than a pronounced change in the formal Ti oxidation state.

Taken together, the XPS results support the mechanism proposed from FTIR and outgassing analysis. Exposure consumes the sp^2 C/C=C-rich dienediol-derived organic units, modifies C–O/C–O–Ti bonding environments, increases the relative contribution of high-binding-energy oxidized-carbon environments within the remaining carbon signal, and redistributes the oxygen coordination environment within the Ti–organic network. In particular, the increased Ti-coordinated O contribution and decreased C–O/Ti–O–C-related contribution in the O 1s spectra are consistent with partial conversion of the organic-rich Ti–O–C environment into a more Ti–O-rich local network. These changes reduce the solubility of the exposed region and contribute to the negative-tone response of Ti–DVG [10, 17, 19]. The repeated-scan XPS results show the same qualitative trend under continuous low-dose X-ray irradiation, further supporting the reliability of the assigned carbon- and oxygen-environment evolution (Figure S6). Sequential C

Just Accepted

1s fitting during repeated XPS irradiation further illustrates the gradual decrease in the C–O-related contribution and the slight increase in the high-binding-energy oxidized-carbon contribution (Figure S7).

Coupled Organic–Inorganic Conversion Mechanism

Raman spectroscopy was used as an additional qualitative probe of possible inorganic-network evolution after exposure. As shown in Figure 6a, the spectra are dominated by the intense Si substrate peak near 520 cm $^{-1}$, which is not assigned to the Ti–DVG film. The enlarged low-wavenumber region shows a weak exposure-associated change that is consistent with increased local Ti–O connectivity. Because the film-related Raman response is weak and no crystalline TiO_2 phase is identified, the Raman data are treated as supporting evidence only and are not used to establish a crystalline phase or an independent mechanistic assignment.

Just Accepted

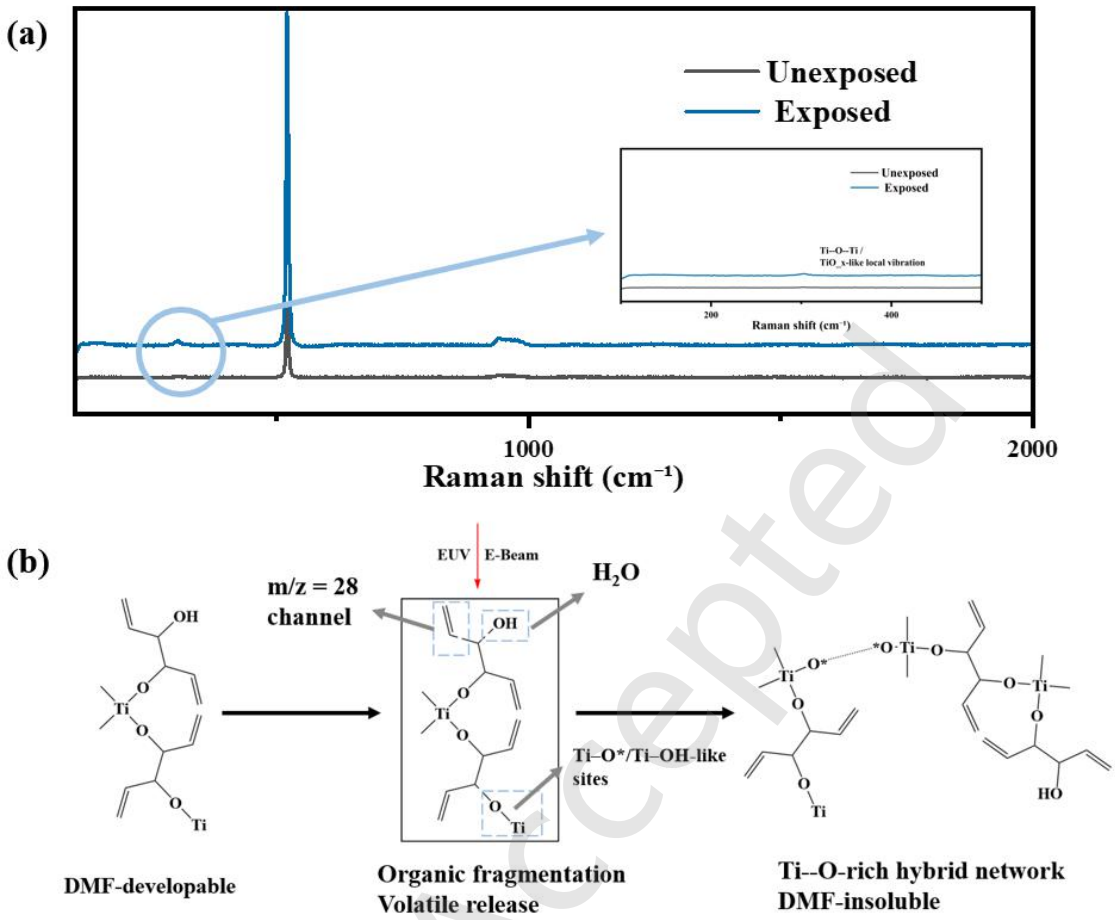


Figure 6. Raman spectra and proposed exposure-induced conversion mechanism of Ti–DVG. (a) Raman spectra of Ti–DVG before and after exposure. The intense peak near 520 cm $^{-1}$ is assigned to the Si substrate, while the enlarged low-wavenumber region highlights weak Ti–O-related vibrational features. (b) Proposed coupled organic–inorganic conversion mechanism of Ti–DVG. Upon irradiation, dienediol-derived C=C environments are consumed or transformed, while C–O/Ti–O–C linkages undergo cleavage or rearrangement. These processes are accompanied by volatile-species evolution, including an exposure-induced $m/z = 28$ channel, and may generate Ti–O *- or Ti–OH-like sites. No unique molecular product is assigned to the $m/z = 28$ signal. Subsequent recombination or condensation of Ti–O-containing sites may promote Ti–O–Ti/TiO $_x$-like local connectivity, producing a more Ti–O-rich hybrid network with reduced solubility in DMF.

On the basis of the complementary FTIR, background-subtracted outgassing, and XPS results, with Raman providing additional qualitative support, the exposure-induced conversion of Ti–DVG is proposed to proceed through a coupled organic–inorganic process (Figure 6b). In the unexposed state, Ti–DVG consists of a Ti–organic hybrid network containing Ti–O–C linkages and dienediol-derived C=C units. Under e-beam or EUV irradiation, the unsaturated C=C environments are consumed or transformed, potentially including partial fragmentation, while C–O/Ti–O–C linkages undergo cleavage or rearrangement [10–12, 26]. These transformations are

Just Accepted

accompanied by volatile-species evolution. In particular, the background-subtracted outgassing spectrum contains an exposure-induced differential channel at $m/z = 28$. Because isobaric species cannot be uniquely distinguished at the available mass resolution, this signal is used as evidence of volatile release rather than as identification of a unique molecular product.

The cleavage or rearrangement of Ti–O–C and C–O environments can leave behind Ti–O * or Ti–OH-like sites within the film. These Ti–O-containing sites can subsequently recombine or condense to form Ti–O–Ti/TiO $_{x}$-like local connectivity. In this process, part of the oxygen-containing organic environment is released as volatile fragments, while another fraction remains in the film as Ti-coordinated oxygen. This interpretation is consistent with the XPS observation of carbon-environment evolution, the increased Ti-coordinated O contribution in the O 1s spectra, and the largely unchanged Ti(IV)-like Ti 2p features.

Therefore, the negative-tone response of Ti–DVG is proposed to arise from a cooperative conversion pathway involving ligand transformation, possible organic fragmentation, volatile release, and increased Ti–O connectivity. The exposed region is proposed to evolve from a relatively organic-rich Ti–O–C hybrid network toward a more Ti–O-rich hybrid network with enhanced Ti–O–Ti/TiO $_{x}$-like local connectivity [12, 19, 20]. The resulting inorganic-enriched network is less soluble in DMF and remains after development, while the unexposed Ti–DVG is removed.

The present data do not quantitatively deconvolute the individual contributions of organic-unit transformation and Ti–O-network condensation to the solubility change. In addition, because a saturated-diol control was not included, the specific contribution of the terminal C=C groups cannot be isolated from other ligand transformations and changes within the Ti–O network. Figure 6 therefore represents a working mechanistic model consistent with the combined spectroscopic and outgassing observations rather than a uniquely established reaction sequence.

Conclusion

In summary, we have developed a molecular-layer-deposited Ti–DVG hybrid photoresist for high-resolution nanoscale lithography. The material combines vapor-phase film formation, titanium-containing inorganic nodes, and dienediol-derived unsaturated organic units in a single hybrid network. The Ti–DVG film shows nearly linear MLD growth, smooth continuous

Just Accepted

morphology, and negative-tone solubility switching after electron-beam exposure and development. These properties enable continuous 25 nm line/space EBL patterns with LER values of 2.347–2.959 nm and EUV interference patterns with half-pitches down to 15–18 nm. Low-contrast limiting EBL features down to approximately 5.2 nm were additionally observed under size-specific exposure and film-thickness conditions. Preliminary etch-transfer results further indicate that the exposed Ti–DVG network provides useful resistance for nanoscale pattern transfer.

Mechanistic characterization supports a proposed coupled organic–inorganic conversion pathway for the lithographic response. Background-corrected FTIR spectra and background-subtracted outgassing measurements show exposure-correlated spectral changes and volatile-species evolution, while XPS and repeated-scan XPS show carbon-environment evolution and redistribution toward more Ti-coordinated oxygen environments. The weak exposure-associated Raman changes are qualitatively consistent with changes in Ti–O-related local connectivity, while the principal mechanistic evidence is provided by the complementary FTIR, background-subtracted outgassing, and XPS results. Together, these results suggest that irradiation converts the initially organic-rich Ti–O–C hybrid network into a more Ti–O-rich, less soluble structure.

This study demonstrates that molecular layer deposition can be used not only to fabricate ultrathin vapor-phase photoresists, but also to incorporate irradiation-transformable organic functionality into metal–organic hybrid networks. The Ti–DVG system therefore provides a mechanistically traceable platform for designing dry photoresists for electron-beam and EUV nanolithography [16, 18].

Experimental

Materials

Tetrakis(dimethylamido)titanium (TDMAT) was purchased from Aimouyuan. 1,5-Hexadiene-3,4-diol (DVG) was purchased from Aladdin. Si(100) wafers were purchased from Sage Electronic Technology Co. Before deposition, the substrates were ultrasonically cleaned in ethanol for 15 min to remove surface contaminants.

Just Accepted

Molecular Layer Deposition of Ti–DVG Films

Ti–DVG films were deposited using an ALD-150D system purchased from Ke-Micro. TDMAT was maintained at 45 °C, and the DVG source vial was heated to 80 °C. The reactor temperature was kept at 120 °C, and dry N_2 was used as the purge gas at a flow rate of 20 sccm. Each MLD cycle consisted of two half-cycles: (i) a 50 ms TDMAT pulse followed by a 20 s N_2 purge and (ii) a 100 ms DVG pulse followed by a 40 s N_2 purge.

Electron-Beam and EUV Lithography

Electron-beam lithography was performed using a CABL-9000C system at 50 keV and 100 pA. Exposure patterns were designed using CAD software. After exposure, the samples were baked at 95 °C for 45 s. DMF was used as the negative-tone developer, with a development time of 30 s. EUV interference lithography was conducted at Beamline BL08U1B of the Shanghai Synchrotron Radiation Facility and at the Hefei light source.

Characterization

FTIR spectra were collected from Ti–DVG films deposited on Si substrates coated with an approximately 100 nm Au layer to enhance the thin-film signal. Before each sample measurement, a background spectrum was acquired under the same instrumental conditions and automatically subtracted. The unexposed and exposed spectra were collected using identical acquisition parameters.

Outgassing analysis was performed using a quadrupole mass-spectrometric detector coupled to the irradiation chamber. A background mass spectrum was acquired before irradiation under otherwise identical instrumental conditions and was subtracted from the spectrum collected during exposure. No N_2 was intentionally introduced into the exposure chamber during the measurement. Because isobaric species cannot be uniquely distinguished at the available mass resolution, no unique molecular assignment was made for individual mass channels, particularly $m/z = 28$.

Raman spectra of the unexposed and exposed Ti–DVG films were collected using identical acquisition conditions. Because the film-related response was weak and the spectra were dominated by the Si substrate signal, the Raman results were interpreted qualitatively.

Just Accepted

X-ray photoelectron spectroscopy (XPS) was performed using a Thermo Scientific K-Alpha spectrometer with an analysis area of approximately 400 μm in diameter. Survey spectra and high-resolution C 1s, O 1s, and Ti 2p spectra were collected to evaluate the elemental composition and chemical bonding evolution of Ti–DVG before and after exposure. Peak fitting was performed using consistent background, peak-position, and line-shape constraints for the unexposed and exposed samples. The fitted component areas were interpreted as relative chemical-state trends rather than absolute quantitative values.

For the repeated-scan XPS validation experiment, the same Ti–DVG region was continuously scanned under vacuum without air exposure, additional light exposure, or wet processing between scans. During XPS acquisition, the incident X-rays generated photoelectrons for chemical-state analysis while also providing a weak accumulated irradiation dose to the radiation-sensitive photoresist film. The sequential C 1s and O 1s spectra were used to monitor early-stage X-ray-induced chemical evolution and to cross-validate the exposure-induced trends observed in the ex situ before/after-exposure XPS measurements.

Film thickness was measured using a homemade ellipsometer. SEM imaging was performed using a Crossbeam 350 system operated at 2 keV. Line critical dimension and line-edge roughness values were extracted from SEM images using the SMILE analysis workflow. AFM characterization was performed using a Bruker Dimension Icon system in closed-loop mode with an R3 probe.

Author information

Corresponding authors

Zhenjiang Li – Shanghai Synchrotron Radiation Facility, Shanghai Institute of Applied Physics, Chinese Academy of Sciences, Shanghai 201204, China; Email: lizhenjiang@sari.ac.cn

Jun Zhao – Shanghai Synchrotron Radiation Facility, Shanghai Institute of Applied Physics, Chinese Academy of Sciences, Shanghai 201204, China; Email: zhaoj@sari.ac.cn

Renzhong Tai – Shanghai Synchrotron Radiation Facility, Shanghai Institute of Applied Physics, Chinese Academy of Sciences, Shanghai 201204, China; Email: tairenzhong@sinap.ac.cn

Just Accepted

Feng Luo – Tianjin Key Lab for Rare Earth Materials and Applications, Center for Rare Earth and Inorganic Functional Materials, School of Materials Science and Engineering, Nankai University, Tianjin 300350, China; Email: feng.luo@nankai.edu.cn Orcid: https://orcid.org/0000-0003-3442-3987

Authors

Yutao Xu – Tianjin Key Lab for Rare Earth Materials and Applications, Center for Rare Earth and Inorganic Functional Materials, School of Materials Science and Engineering, Nankai University, Tianjin 300350, China; Email: 1120230687@mail.nankai.edu.cn

Xingkun Wang – Tianjin Key Lab for Rare Earth Materials and Applications, Center for Rare Earth and Inorganic Functional Materials, School of Materials Science and Engineering, Nankai University, Tianjin 300350, China; Email: 1120220598@mail.nankai.edu.cn

Zhixing Ren - College of Electronic Information and Optical Engineering, Nankai University, Tianjin 300350, China; Email: 2120230384@mail.nankai.edu.cn

Jianan Xie – College of Electronic Information and Optical Engineering, Nankai University, Tianjin 300350, China; Email: xiejn@mail.nankai.edu.cn

Miao Meng – Tianjin Key Lab for Rare Earth Materials and Applications, Center for Rare Earth and Inorganic Functional Materials, School of Materials Science and Engineering, Nankai University, Tianjin 300350, China; Email:mengmiao@nankai.edu.cn

Fanghao Xu – Tianjin Key Lab for Rare Earth Materials and Applications, Center for Rare Earth and Inorganic Functional Materials, School of Materials Science and Engineering, Nankai University, Tianjin 300350, China; Email:2120241499@mail.nankai.edu.cn

Zhaolei Liang – Tianjin Key Lab for Rare Earth Materials and Applications, Center for Rare Earth and Inorganic Functional Materials, School of Materials Science and Engineering, Nankai University, Tianjin 300350, China; Email: 2120231378@mail.nankai.edu.cn

Muhan Tang – Tianjin Key Lab for Rare Earth Materials and Applications, Center for Rare Earth and Inorganic Functional Materials, School of Materials Science and Engineering, Nankai University, Tianjin 300350, China; Email: 1120250264@mail.nankai.edu.cn

Just Accepted

Yazhuo Xie – Tianjin Key Lab for Rare Earth Materials and Applications, Center for Rare Earth and Inorganic Functional Materials, School of Materials Science and Engineering, Nankai University, Tianjin 300350, China; Email: xieyazhuo1@163.com

Author Contributions

Yutao Xu: conceptualization, investigation, data analysis, and writing original draft.

Xingkun Wang: experimental assistance and data analysis.

Zhixing Ren: etch-transfer experiments.

Jianan Xie: LER analysis.

Miao Meng: etch-transfer experiments.

Fanghao Xu: sample characterization.

Zhaolei Liang: sample preparation and characterization.

Muhan Tang: assistance with photoresist preparation.

Yazhuo Xie: sample characterization.

Zhenjiang Li: EUV/XIL analysis and manuscript revision.

Jun Zhao: supervision, experimental assistance, and manuscript revision.

Renzhong Tai: supervision.

Feng Luo: supervision, project administration, and funding acquisition.

Competing interests

The authors declare no competing interests.

Data availability

The data that support the findings of this study are available from the corresponding author upon reasonable request.

Just Accepted

Acknowledgements

This work was supported by the National Key Research and Development Program of China (No. 2021YFA1601003) and the National Natural Science Foundation of China (No. 92461315). The authors thank the Shanghai Synchrotron Radiation Facility BL08U1B (31124.02.SSRF.BL08U1B) and the Photon Science Research Center for Carbon Dioxide for technical support.

Use of AI statement

None

Electronic Supplementary Material

Electronic Supplementary Material is available in the online version of this article and includes supplementary experimental details, dose-response analysis, AFM and SEM images, etch-transfer evaluation, LER analysis workflow, repeated-scan XPS validation, XPS fitting details, additional FTIR and Raman spectra, outgassing analysis, and summary tables for EBL and EUV patterning results.

References

[1] Li, L.; Liu, X.; Pal, S.; Wang, S.; Ober, C. K.; Giannelis, E. P. Extreme ultraviolet resist materials for sub-7 nm patterning. *Chem. Soc. Rev.* **2017**, *46*, 4855-4866. DOI: 10.1039/C7CS00080D.

[2] Li, M.; Aqad, E. Key challenges and opportunities for advanced extreme ultraviolet lithography photoresist materials. *Adv. Funct. Mater.* **2025**, *35*, 2420962. DOI: 10.1002/adfm.202420962.

[3] Develioglu, A.; Vockenhuber, M.; van Lent-Protasova, L.; Mochi, I.; Ekinci, Y.; Kazazis, D. Advancements in EUV photoresists for high-NA lithography. In *Proceedings of the International Conference on Extreme Ultraviolet Lithography 2023*, 2023, Vol. 12750, 1275008. DOI: 10.1117/12.2686250.

Just Accepted

[4] Manouras, T.; Argitis, P. High sensitivity resists for EUV lithography: a review of material design strategies and performance results. *Nanomaterials* **2020**, *10*, 1593. DOI: 10.3390/nano10081593.

[5] Kang, Y. K.; Lee, S. J.; Eom, S.; Kim, B. G.; Hwang, C.-C.; Kim, M.-G. Recent progress of inorganic photoresists for next-generation EUV lithography. *J. Mater. Chem. C* **2024**, *12*, 15855-15887. DOI: 10.1039/D4TC02671C.

[6] Wang, Z.; Chen, J.; Yu, T.; Zeng, Y.; Yang, G.; Allenet, T.; Vockenhuber, M.; Ekinci, Y.; Li, Y. Water developable non-chemically amplified photoresist for electron beam and extreme ultraviolet lithography. *J. Micro/Nanopattern. Mater. Metrol.* **2022**, *21*, 041403. DOI: 10.1117/1.JMM.21.4.041403.

[7] Tao, P.; Sheng, L.; Wang, Q.; Cui, H.; Wang, X.; He, X.; Xu, H. Photoresist for extreme ultraviolet lithography. In *Proceedings of the 2020 International Workshop on Advanced Patterning Solutions (IWAPS)*, 2020, pp 1-4. DOI: 10.1109/IWAPS51164.2020.9286794.

[8] Fallica, R.; Haitjema, J.; Wu, L.; Castellanos, S.; Brouwer, A. M.; Ekinci, Y. Absorption coefficient of metal-containing photoresists in the extreme ultraviolet. *J. Micro/Nanolithogr. MEMS MOEMS* **2018**, *17*, 023505. DOI: 10.1117/1.JMM.17.2.023505.

[9] Lim, G.; Lee, K.; Koh, C.; Nishi, T.; Yoon, H. J. Multinuclear tin-based macrocyclic organometallic resist for EUV photolithography. *ACS Mater. Au* **2024**, *4*, 468-478. DOI: 10.1021/acsmaterialsau.4c00010.

[10] Evrard, Q.; Sadegh, N.; Mathew, S.; Zuidinga, E.; Watts, B.; Paradiz Dominguez, M.; Giglia, A.; Mahne, N.; Nannarone, S.; Nishimura, A.; et al. Extreme ultraviolet photoresponse of organotin-based photoresists with borate counteranions. *ACS Appl. Mater. Interfaces* **2024**, *16*, 42947-42956. DOI: 10.1021/acsami.4c08636.

[11] Ma, J. H.; Needham, C.; Wang, H.; Neureuther, A.; Prendergast, D.; Naulleau, P. Mechanistic advantages of organotin molecular EUV photoresists. *ACS Appl. Mater. Interfaces* **2022**, *14*, 5514-5524. DOI: 10.1021/acsami.1c12411.

[12] Li, J.; Wang, Z.; Wang, H. Computational study of organotin oxide systems for extreme ultraviolet photoresist. *J. Phys. Chem. A* **2025**, *129*, 1420-1428. DOI: 10.1021/acs.jpca.4c07585.

Just Accepted

[13] Qiao, Y.; Shi, G.; Zhang, O.; Li, Y.; Vockenhuber, M.; Ekinci, Y.; Luo, F.; Zhang, L. Heterometallic Ti-Zr oxo nanocluster photoresists for advanced lithography. *Sci. China Mater.* **2024**, *67*, 3132-3141. DOI: 10.1007/s40843-024-3013-9.

[14] Zhou, R.; Cao, M.; Tan, Y.; Neisser, M.; Xu, H. Polytelluoxane as the ideal formulation for EUV photoresist. *Sci. Adv.* **2025**, *11*, eadx1918. DOI: 10.1126/sciadv.adx1918.

[15] Zhang, R.-S.; Miao, L.; Lu, X.-Y.; Li, Q.; Luo, F.; Qiu, H.-Y.; Wu, G.-P. Norbornene and epoxide-substituted silsesquioxane photoresists with high-sensitivity and stability. *ACS Nano* **2025**, *19*, 38243-38254. DOI: 10.1021/acsnano.5c06472.

[16] Jung, J.; Park, R.; Jeon, N. Vacuum-processed hybrid resists for advanced lithography: molecular layer deposition and sequential infiltration synthesis. *Nanoscale* **2026**, *18*, 4064-4073. DOI: 10.1039/D5NR04721H.

[17] Seok, J.-H.; Kim, J.; Ji, H.; Lee, J.; Lee, T.; Yoon, K.-S.; Sung, M. M.; Ahn, J. Vapor-phase dry development of a nanoscale Zn-based metal-organic extreme ultraviolet photoresist via surface-limited β-diketone chelation for high-resolution patterning. *ACS Appl. Nano Mater.* **2026**, *9*, 5506-5515. DOI: 10.1021/acsanm.6c00102.

[18] Multia, J.; Karppinen, M. Atomic/molecular layer deposition for designer's functional metal-organic materials. *Adv. Mater. Interfaces* **2022**, *9*, 2200210. DOI: 10.1002/admi.202200210.

[19] Shi, J.; Ravi, A.; Richey, N. E.; Gong, H.; Bent, S. F. Molecular layer deposition of a hafnium-based hybrid thin film as an electron beam resist. *ACS Appl. Mater. Interfaces* **2022**, *14*, 27140-27148. DOI: 10.1021/acsami.2c04092.

[20] Lee, W.-I.; Le, D. N.; Yen, M.; Lin, M.; Subramanian, A.; Tong, X.; Tiwale, N.; Kim, J.; Nam, C.-Y. Molecular layer deposited aluminum-based hybrid resist for high-resolution nanolithography and direct ultra-high aspect ratio pattern transfer. *Adv. Mater. Technol.* **2026**, *11*, e01639. DOI: 10.1002/admt.202501639.

[21] Yang, K.; Xu, H.; Sakai, K.; Kosma, V.; Giannelis, E. P.; Ober, C. K. Radical sensitive zinc-based nanoparticle EUV photoresists. In *Advances in Patterning Materials and Processes XXXVI*; Proceedings of SPIE, 2019, Vol. 10960, 109601R. DOI: 10.1117/12.2514982.

Just Accepted

[22] Gangnaik, A. S.; Georgiev, Y. M.; Holmes, J. D. New generation electron beam resists: a review. *Chem. Mater.* **2017**, *29*, 1898-1917. DOI: 10.1021/acs.chemmater.6b03483.

[23] Li, C.-D.; Lin, T.-A.; Lin, B.-J.; Chen, P.-H.; Chen, S.-Z.; Chiu, P.-W.; Liu, R.-S. Enhanced edge etching resistance and EUV lithographic performance of a tin-oxide photoresist via a blend strategy. *ACS Appl. Nano Mater.* **2025**, *8*, 18401-18414. DOI: 10.1021/acsanm.5c03131.

[24] Li, Z.-J.; Qi, C.-H.; Li, B.-N.; Yang, S.-M.; Zhao, J.; Lei, Z.-D.; Zhu, S.-J.; Shi, H.; Wang, L.; Wu, Y.-Q.; et al. Latest developments in EUV photoresist evaluation capability at Shanghai Synchrotron Radiation Facility. *Nucl. Sci. Tech.* **2023**, *34*, 198. DOI: 10.1007/s41365-023-01351-8.

[25] Zhao, Y.; Huang, X.; Si, Y.; Zheng, L.; Chen, H.; Zhao, J.; Luo, F.; Zhang, J.; Chen, P.; Peng, X. Additive-assisted forming high-quality thin films of Sn-oxo cluster for nanopatterning. *ACS Appl. Mater. Interfaces* **2024**, *16*, 41659-41668. DOI: 10.1021/acsami.4c06230.

[26] Chen, H.; Huang, X.; Zhao, Y.; Zhao, J.; Chen, P.; Peng, X. Balancing sensitivity and resolution by feedback regulation of free radicals from Sn-C bonds in tin-oxygen clusters EBL photoresist. *Sci. China Mater.* **2024**, *67*, 3142-3150. DOI: 10.1007/s40843-024-3062-y.

[27] Bespalov, I.; Zhang, Y.; Haitjema, J.; Tromp, R. M.; van der Molen, S. J.; Brouwer, A. M.; Jobst, J.; Castellanos, S. Key role of very low energy electrons in tin-based molecular resists for extreme ultraviolet nanolithography. *ACS Appl. Mater. Interfaces* **2020**, *12*, 9881-9889. DOI: 10.1021/acsami.9b19004.

[28] Biesinger, M. C. Accessing the robustness of adventitious carbon for charge referencing (correction) purposes in XPS analysis: insights from a multi-user facility data review. *Appl. Surf. Sci.* **2022**, *597*, 153681. DOI: 10.1016/j.apsusc.2022.153681.

Just Accepted

Electronic Supplementary Material

Molecularly deposited titanium–dienediol hybrid photoresists for high-resolution electron-beam and EUV lithography

Yutao Xu[1,3], Xingkun Wang[1], Zhixing Ren[2], Jianan Xie[2,3], Miao Meng[1], Fanghao Xu[1], Zhaolei Liang[1], Muhan Tang[1], Yazhuo Xie[1], Zhenjiang Li[3,*], Jun Zhao[3,*], Renzhong Tai[3,*], and Feng Luo[1,2,3,*]

[1] Tianjin Key Lab for Rare Earth Materials and Applications, Center for Rare Earth and Inorganic Functional Materials, Smart Sensor Interdisciplinary Science Center, School of Materials Science and Engineering, Nankai University, Tianjin 300350, China

[2] College of Electronic Information and Optical Engineering, Nankai University, Tianjin 300350, China

[3] Shanghai Synchrotron Radiation Facility, Shanghai Institute of Applied Physics, Chinese Academy of Sciences, Shanghai 201204, China

[*] Address correspondence to Zhenjiang Li, lizhenjiang@sari.ac.cn; Jun Zhao, zhaoj@sari.ac.cn; Renzhong Tai, tairenzhong@sinap.ac.cn; Feng Luo, feng.luo@nankai.edu.cn

Supporting information to https://doi.org/10.26599/NR.2026.94909246

Contents

Materials and Methods
Dose-Response Analysis
  Extraction of D 10, D 50, D 90, and Contrast
Supplementary Figures
  EBL Dose Matrix
  Additional AFM Morphology of As-Deposited Ti–DVG Films
  Additional EBL Patterns with Different Feature Sizes and Duty Ratios
  Enlarged SEM Images of Limiting-Resolution EBL Patterns
  Preliminary Etch-Transfer Evaluation
XPS Fitting Parameters
  Repeated-Scan XPS Validation of Exposure-Induced Chemical Evolution
  Sequential C 1s Fitting during Repeated XPS Irradiation
SEM Image Selection and LER Analysis

Just Accepted

Materials and Methods

Detailed experimental conditions are provided in the Experimental section of the main text. Additional information related to dose-response extraction, SEM image analysis, LER evaluation, repeated-scan XPS validation, and supplementary patterning results is provided below.

Unless otherwise stated, Ti–DVG films with a nominal target thickness of approximately 30 nm were used for lithographic evaluation. For the limiting-resolution EBL experiments, the 17.65 nm feature was obtained using an approximately 30 nm-thick film, whereas the 7.90 and 5.24 nm features were obtained using thinner films with a nominal target thickness of approximately 10 nm. The thinner-film conditions were used for the sub-10 nm resolution tests to reduce the resist volume and improve pattern stability at these dimensions. Electron-beam lithography was performed using a CABL-9000C system operated at 50 keV and 100 pA. After exposure, the samples were baked at 95 °C for 45 s and developed in DMF for 30 s. EUV interference lithography was conducted at Beamline BL08U1B of the Shanghai Synchrotron Radiation Facility and at the Hefei light source. The reported EUV exposure doses were corrected by the corresponding grating efficiency.

Dose-Response Analysis

Extraction of D_{10}, D_{50}, D_{90}, and Contrast

The normalized remaining thickness was calculated as

$$\frac{T}{T_0}, \qquad \text{(S1)}$$

where T is the remaining film thickness after exposure, post-exposure bake, and development, and T_0 is the reference retained thickness used for normalization.

The dose values D_{10}, D_{50}, and D_{90} were extracted from the normalized dose-response curve at T/T_0 = 0.1, 0.5, and 0.9, respectively. Linear interpolation between adjacent data points was used when the target normalized thickness fell between two measured dose points.

The contrast was calculated using

$$\gamma = \left[\log_{10}\left(\frac{D_{90}}{D_{10}}\right)\right]^{-1}. \qquad \text{(S2)}$$

For the representative Ti–DVG dose-response curve shown in the main text, the extracted values are summarized in Table S1.

Table S1. Dose-response parameters extracted from the normalized remaining-thickness curve of Ti–DVG.

Parameter	Value
D_{10}	105.9 μC cm^{-2}
D_{50}	310.9 μC cm^{-2}

Just Accepted

Parameter	Value
D_{90}	858.3 μC cm^{-2}
γ	1.10

Supplementary Figures

EBL Dose Matrix

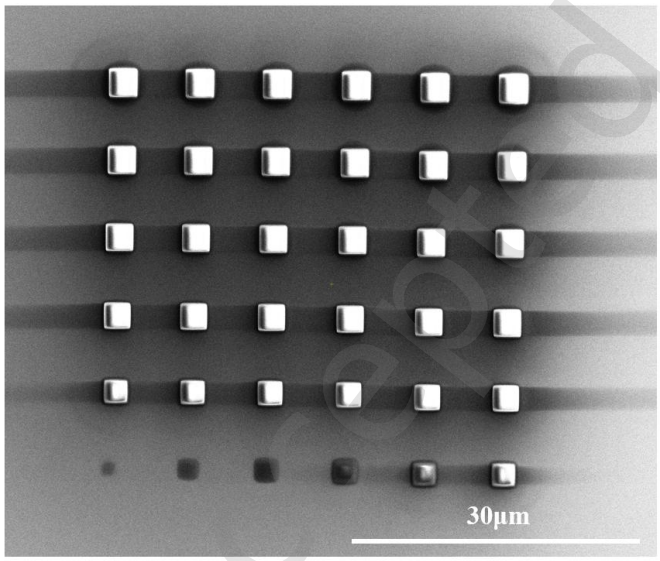


Figure S1. Representative EBL dose matrix of Ti–DVG. The square-array pattern was exposed with a stepwise dose gradient from 300 to 1800 μC cm^{-2} with an increment of 60 μC cm^{-2}. The gradual increase in retained pattern height with exposure dose supports the negative-tone dose-response behavior discussed in the main text.

Just Accepted

Additional AFM Morphology of As-Deposited Ti–DVG Films

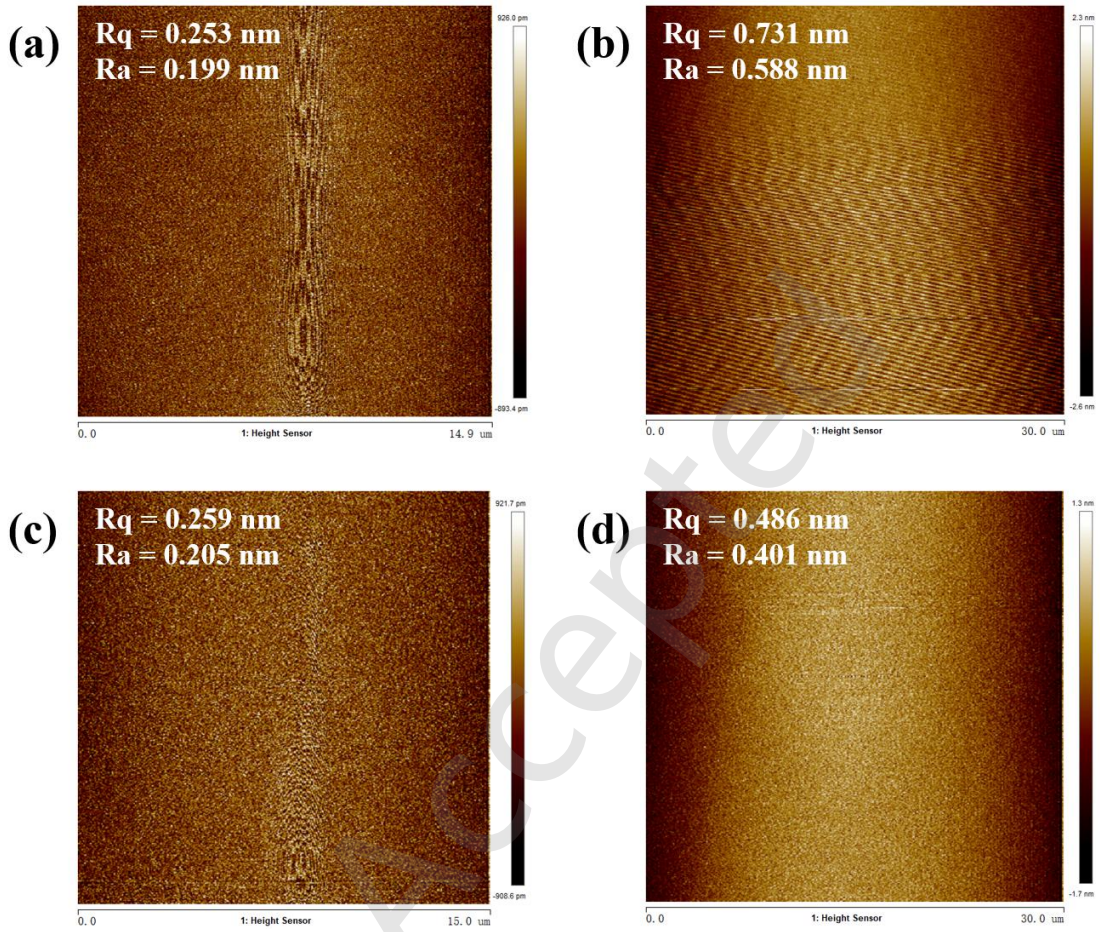


Figure S2. Additional AFM height images of as-deposited Ti–DVG films. (a,c) AFM images recorded over approximately 15 μm scan regions, showing Rq/Ra values of 0.253/0.199 nm and 0.259/0.205 nm, respectively. (b,d) AFM images recorded over approximately 30 μm scan regions, showing Rq/Ra values of 0.731/0.588 nm and 0.486/0.401 nm, respectively. The sub-nanometer roughness values obtained from different scan regions confirm the smooth and continuous morphology of the molecularly deposited Ti–DVG films.

Just Accepted

Additional EBL Patterns with Different Feature Sizes and Duty Ratios

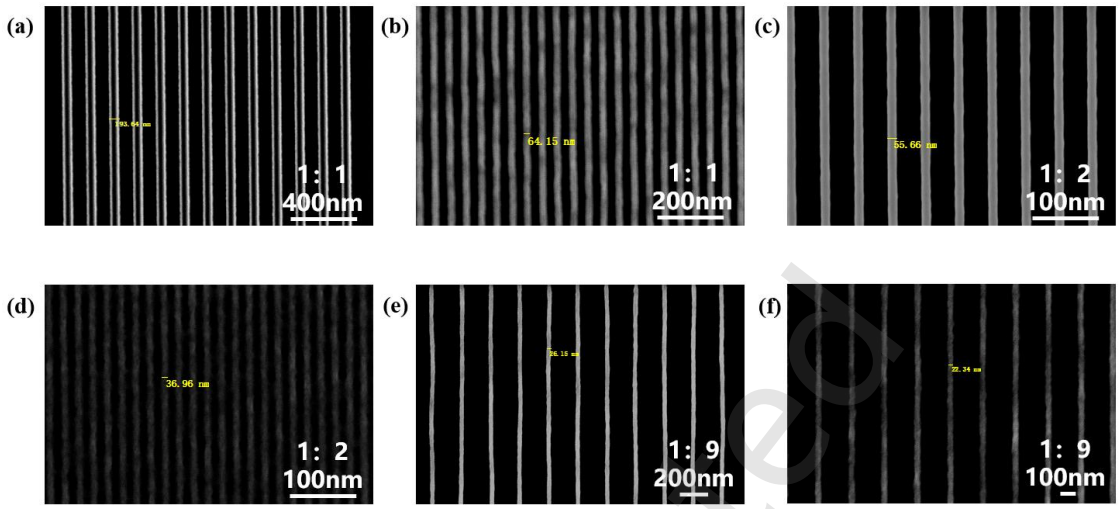


Figure S3. Additional electron-beam lithographic patterns of Ti–DVG obtained with different line/space ratios and feature sizes. (a,b) Dense 1:1 line/space patterns with measured periodic distances of 193.64 and 64.15 nm, respectively. (c,d) 1:2 line/space patterns with measured feature distances of 55.66 and 36.96 nm, respectively. (e,f) High-duty-ratio 1:9 line/space patterns with measured line widths of 22.15 and 22.34 nm, respectively. These additional SEM images demonstrate that Ti–DVG can be patterned over a range of feature sizes and duty ratios, supporting the general nanoscale patternability of the resist beyond the representative high-resolution and limiting-resolution examples shown in the main text.

Enlarged SEM Images of Limiting-Resolution EBL Patterns

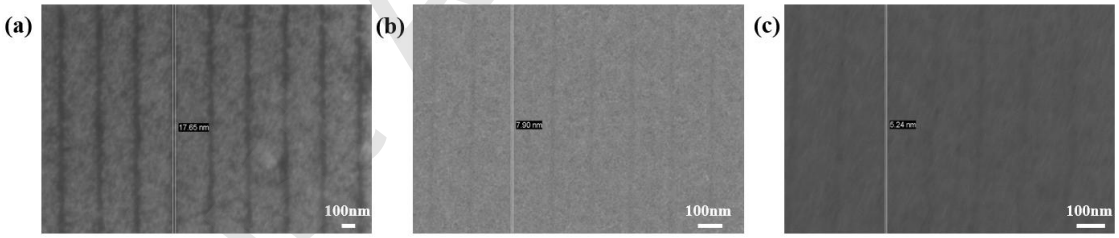


Figure S4. Enlarged SEM images and line-width measurements of limiting-resolution electron-beam lithographic patterns of Ti–DVG. (a–c) Enlarged views corresponding to the ultrafine features shown in Figure 2d–f of the main text, with measured critical dimensions of 17.65, 7.90, and 5.24 nm, respectively. The 17.65 nm feature was obtained using an approximately 30 nm-thick Ti–DVG film, whereas the 7.90 and 5.24 nm features were obtained using thinner films with a nominal target thickness of approximately 10 nm. The smaller retained resist volume in the sub-10 nm tests likely contributes to the reduced SEM material contrast. These images are therefore presented as limiting-feature demonstrations rather than as quantitative LER measurements.

Just Accepted

Preliminary Etch-Transfer Evaluation

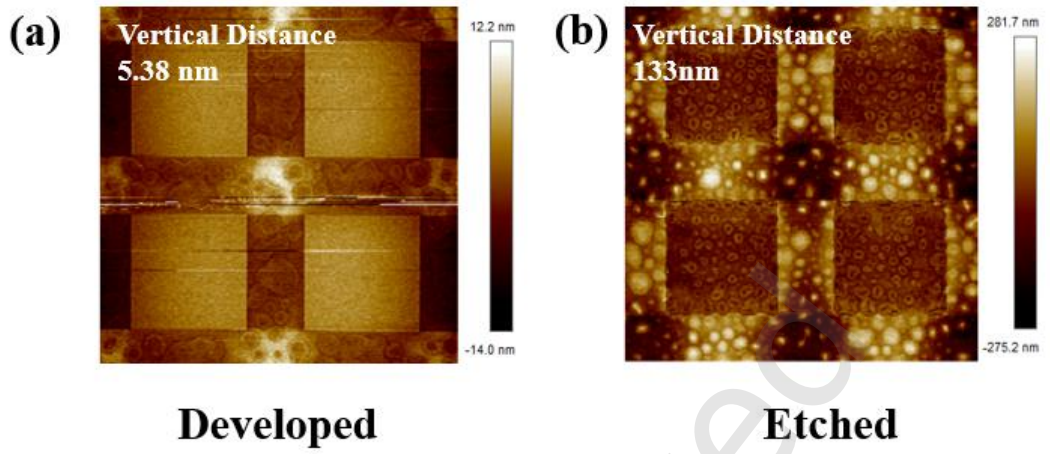


Figure S5. Preliminary etch-transfer evaluation of Ti–DVG. (a) AFM height image of the developed Ti–DVG pattern, showing a vertical distance of 5.38 nm. (b) AFM height image after etching, showing a vertical relief of approximately 133 nm after plasma processing. The substantial transferred relief provides a preliminary demonstration that the patterned Ti–DVG layer can function as an etch-resistant mask under the tested conditions.

Table S2. ICP etching conditions used for the preliminary pattern-transfer evaluation of Ti–DVG.

Process	Temperature (°C)	Pressure (mTorr)	ICP power (W)	RF power (W)	Gas flow rate (sccm)	Etching time (s)	Substrate
Bosch	20	15	400	20	C_4F_8: 30 7s; SF_6: 15 5s	**12**	**Si(100)**

The ICP conditions used for the preliminary pattern-transfer experiment are summarized in Table S2. The etch-transfer result shown in Figure S5 was obtained using the same plasma recipe.

XPS Fitting Parameters

The C 1s, O 1s, and Ti 2p spectra of Ti–DVG were fitted using Thermo Scientific Avantage with the Smart background and Gaussian–Lorentzian product peak shapes. The binding energy scale was referenced to the C 1s C–C component at 284.80 eV for both the unexposed and exposed samples. Component assignments and initial peak positions were guided by the reference binding energies and spectral interpretation guidelines provided in the Thermo Scientific XPS Periodic Table. The same referencing procedure and assignment scheme were applied to both conditions.

Component positions, widths, and intensities were manually initialized before numerical optimization using the Powell algorithm. The maximum number of iterations was 100, and the convergence setting was 0.001. The same background type, peak-shape model, and FWHM fitting-parameter limits were used for the unexposed and exposed spectra. The software FWHM fitting-parameter limits were 0.7–2 eV for C 1s and 0.5–3.5 eV for O 1s and Ti 2p.

Table S3 summarizes the fitted binding energies, full widths at half maximum (FWHM), relative component areas, and working assignments before and after electron-beam exposure. The relative area of

Just Accepted

each component is expressed as a percentage of the total fitted component area within the corresponding core-level region.

Table S3. Fitted XPS component parameters for Ti–DVG before and after electron-beam exposure. Binding energies and FWHM values are reported in eV. Relative areas are normalized to the total fitted component area within the corresponding core-level region. Component assignments represent working interpretations of the fitted spectral contributions.

Core level	Working assignment	Binding energy (eV)	FWHM (eV)	area (%)
Before exposure				
C 1s	C sp^3 / C–C	284.80	1.50	47.30
C 1s	C sp^2 / C=C	284.31	1.40	19.22
C 1s	C–O / C–O–Ti	286.21	1.08	32.27
C 1s	High-binding-energy oxidized carbon	288.70	1.22	1.21
O 1s	Ti-coordinated O	530.63	1.71	11.14
O 1s	C–O / Ti–O–C-related O	531.79	1.52	60.79
O 1s	O–H / adsorbed-O-related contribution	532.76	1.98	28.08
Ti 2p	Ti $2p_{3/2}$	458.91	1.62	66.61
Ti 2p	Ti $2p_{1/2}$	464.64	2.24	33.39
After exposure				
C 1s	C sp^3 / C–C	284.80	1.46	56.03
C 1s	C sp^2 / C=C	284.32	1.32	11.83
C 1s	C–O / C–O–Ti	286.27	1.11	27.50
C 1s	High-binding-energy oxidized carbon	288.70	1.65	4.64
O 1s	Ti-coordinated O	530.49	1.76	18.27
O 1s	C–O / Ti–O–C-related O	531.90	1.59	50.47
O 1s	O–H / adsorbed-O-related contribution	532.71	1.96	31.26
Ti 2p	Ti $2p_{3/2}$	458.88	1.42	67.39
Ti 2p	Ti $2p_{1/2}$	464.60	2.09	32.61

Interpretation of the fitted components. The C 1s assignments represent broad carbon bonding environments within the hybrid film. The two lower-binding-energy components assigned to C sp^3/C–C and C sp^2/C=C overlap strongly in the unexposed spectrum. Their individual fitted areas should therefore be interpreted as model-dependent spectral contributions. The high-binding-energy component is assigned broadly to oxidized carbon rather than to a unique carbonyl-containing molecular species.

The O 1s region contains overlapping contributions from Ti–O, Ti–O–C, C–O, hydroxyl groups, and adsorbed oxygen-containing species. The three fitted components are used to compare the relative distribution of oxygen environments before and after exposure, rather than to independently quantify each

Just Accepted

oxygen species. In particular, the Ti-coordinated-O contribution alone does not establish crystalline TiO_2 formation, and the higher-binding-energy components do not provide an independent quantitative measure of carbonyl oxygen.

The Ti 2p spectra are represented by the Ti $2p_{3/2}$ and Ti $2p_{1/2}$ components. The fitted binding energies listed in Table S3 give spin–orbit separations of 5.73 eV before exposure and 5.72 eV after exposure. These values describe the fitted results rather than prescribed separation constraints.

Overall, the fitted component fractions support comparative interpretation of exposure-associated spectral changes. They are not interpreted as absolute chemical-state populations or as unique identification of individual molecular species.

Repeated-Scan XPS Validation of Exposure-Induced Chemical Evolution

To further cross-validate the exposure-induced chemical evolution of Ti–DVG, a repeated-scan XPS experiment was designed as a tailored in situ-like probe for this radiation-sensitive photoresist. In a conventional XPS measurement, incident X-rays generate photoelectrons that provide chemical-state information. For photoresist films, however, the same X-ray irradiation can also act as a weak exposure source. Although the irradiation imparted during a single XPS scan is limited, repeated XPS acquisition can introduce a cumulative X-ray dose to the radiation-sensitive film.

In this experiment, the same Ti–DVG region was continuously scanned under vacuum without air exposure, additional light exposure, or wet processing between scans. Therefore, the observed spectral evolution reflects a direct response of the film to controlled X-ray irradiation during XPS acquisition. As shown in Figure S6b, repeated scanning leads to limited but measurable changes in the elemental composition, including a slight decrease in carbon content and corresponding increases in oxygen and titanium contributions. The sequential C 1s spectra in Figure S6c show that the C–O-related contribution decreases with increasing scan number, accompanied by a small increase in the high-binding-energy oxidized-carbon contribution. The sequential O 1s spectra in Figure S6d further show increasing low-binding-energy Ti-coordinated oxygen and high-binding-energy O–H/adsorbed-O-related contributions during repeated irradiation. These trends agree well with the ex situ before/after-exposure XPS comparison in the main text, supporting the assignment of exposure-induced C–O/Ti–O–C rearrangement, partial ligand fragmentation, and formation of a more Ti–O-rich local environment.

This repeated-scan XPS experiment therefore serves as an internal cross-validation of the proposed Ti–DVG conversion mechanism. Importantly, the approach does not rely on sample transfer, ambient exposure, or external post-irradiation processing, which minimizes interference from air oxidation, adventitious contamination, and secondary illumination. The method is particularly useful for radiation-sensitive dry photoresists, where XPS acquisition itself can be used in a controlled manner to probe early-stage chemical conversion under vacuum.

Just Accepted

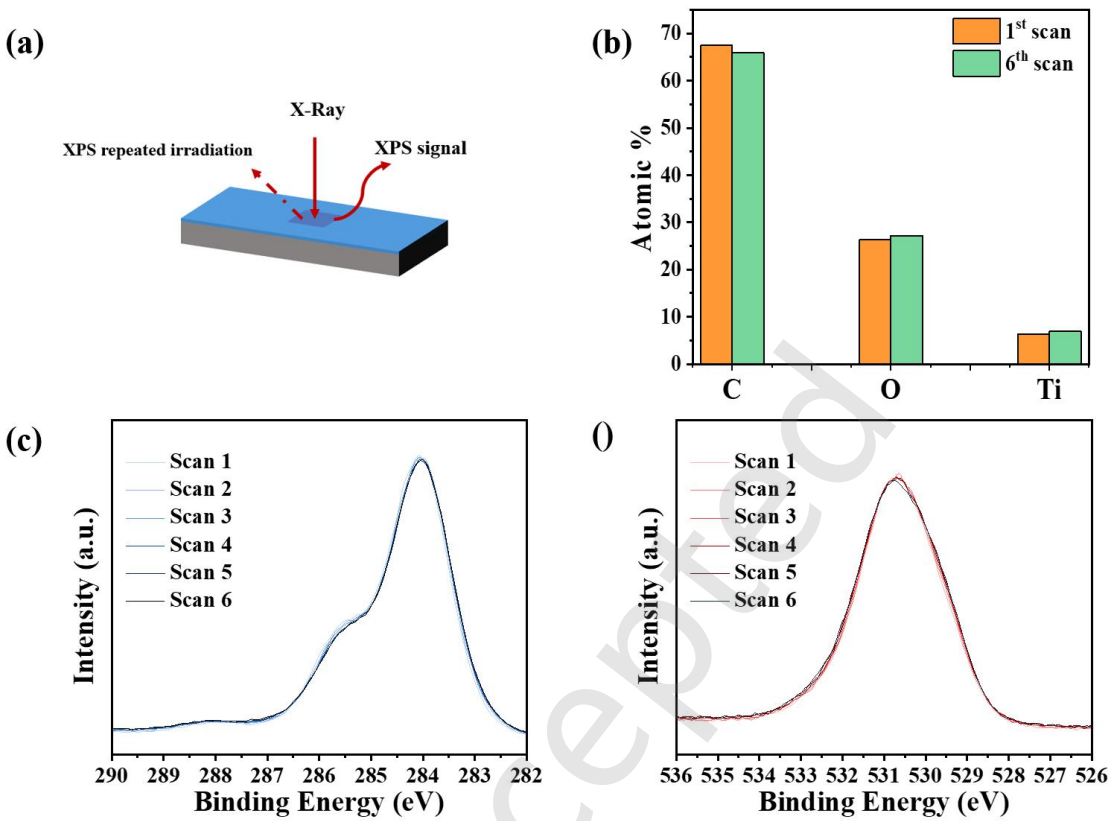


Figure S6. Repeated-scan XPS validation of exposure-induced chemical evolution in Ti–DVG. (a) Schematic illustration of the repeated-scan XPS experiment. During XPS acquisition, the incident Al Kα X-rays simultaneously generate photoelectrons for chemical-state analysis and provide a weak irradiation dose to the photoresist film. (b) Atomic percentages of C, O, and Ti extracted from the first and sixth XPS scans, showing limited but measurable composition changes after repeated X-ray irradiation. (c) Sequential C 1s spectra collected from scan 1 to scan 6. (d) Sequential O 1s spectra collected from scan 1 to scan 6. The repeated scans reveal a gradual decrease in C–O-related carbon signals and a slight increase in high-binding-energy oxidized-carbon contributions, together with an increase in Ti-coordinated/O–H-related oxygen components. These trends are consistent with the before/after-exposure XPS results in the main text and support exposure-induced ligand transformation and oxygen-environment redistribution in Ti–DVG.

Sequential C 1s Fitting during Repeated XPS Irradiation

To further illustrate the carbon-environment evolution during repeated XPS irradiation, the C 1s spectra collected from the first to sixth scans were fitted using the same component assignments. As shown in Figure S7, the C–O-related contribution gradually decreases from 21.72% in the first scan to 19.58% in the sixth scan, while the high-binding-energy oxidized-carbon contribution increases slightly from 3.09% to 3.90%. These trends provide a specific C 1s fitting example supporting the repeated-scan XPS validation in Figure S6 and are consistent with exposure-induced C–O/Ti–O–C rearrangement and redistribution of the residual carbon environments.

Just Accepted

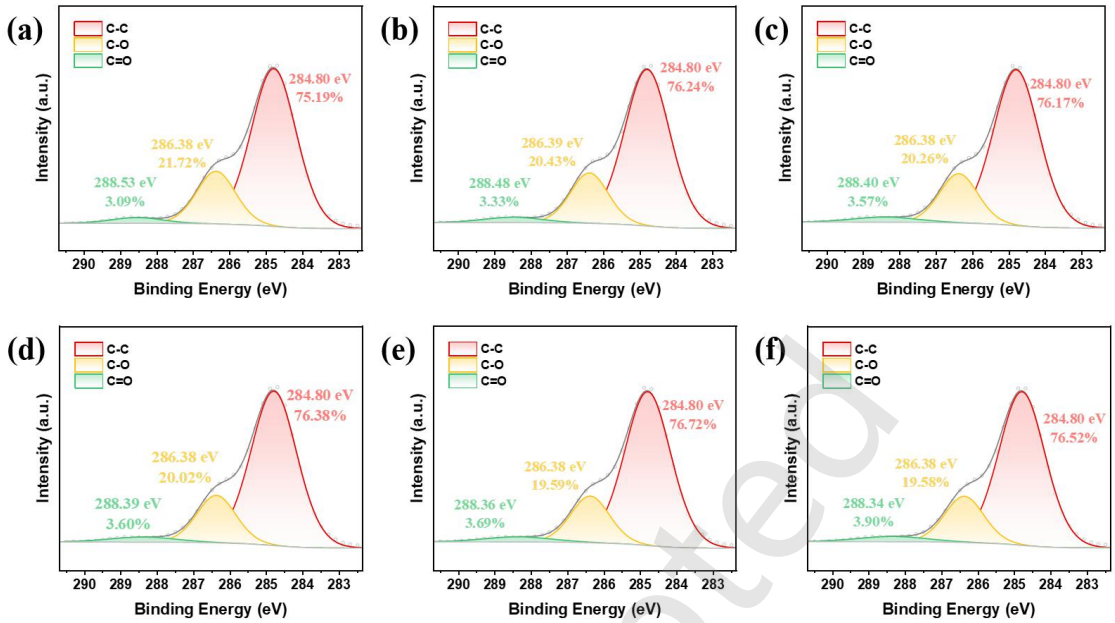


Figure S7. Sequential C 1s fitting results of Ti–DVG during repeated XPS irradiation. (a–f) C 1s spectra collected from the first to sixth XPS scans, respectively, from the same Ti–DVG region under vacuum. The spectra were fitted using C–C, C–O, and high-binding-energy oxidized-carbon components with consistent fitting constraints. During repeated X-ray irradiation, the C–O-related contribution decreases from 21.72% in the first scan to 19.58% in the sixth scan, while the high-binding-energy oxidized-carbon contribution increases slightly from 3.09% to 3.90%. This trend provides a specific C 1s fitting example supporting the repeated-scan XPS validation in Figure S6 and is consistent with exposure-induced ligand rearrangement and redistribution of the residual carbon environments.

Table S4. Representative elemental composition of Ti–DVG before and after exposure, extracted from XPS analysis.

Condition	C 1s (at.%)	O 1s (at.%)	Ti 2p (at.%)	Notes
Before exposure, dataset 1	64.80	30.35	4.85	Representative area
After exposure, dataset 1	60.43	33.32	6.25	Representative area
Before exposure, dataset 2	62.74	31.88	5.38	Repeat area
After exposure, dataset 2	62.22	31.56	6.22	Repeat area

Table S5. Summary of representative EBL patterns shown in Figure 2 of the main text.

Pattern type	Dose (μC cm $^{-2}$)	Nominal feature	Duty ratio	Nominal film thickness	LER
Line/space	2000	HP = 25 nm	1:1	~30 nm	2.347 nm
Line/space	2000	CD = 25 nm	1:2	~30 nm	2.492 nm
Line/space	2000	CD = 25 nm	1:3	~30 nm	2.959 nm
Limiting feature	1500	CD = 17.65 nm	n.a.	~30 nm	n.a.
Limiting feature	2400	CD = 7.90 nm	n.a.	~10 nm	n.a.

Just Accepted

Pattern type	Dose (μC cm $^{-2}$)	Nominal feature	Duty ratio	Nominal film thickness	LER
Limiting feature	3800	CD = 5.24 nm	n.a.	~10 nm	n.a.

Table S6. Summary of representative EUV interference lithography patterns after correction by grating efficiency.

Pattern	Corrected dose (mJ cm $^{-2}$)	Half-pitch	LER
EUV line/space	18.2	HP = 50 nm	22.492 nm
EUV line/space	20.4	HP = 40 nm	19.878 nm
EUV line/space	20.4	HP = 30 nm	19.551 nm
EUV line/space	34.0	HP = 22 nm	18.943 nm
EUV line/space	49.5	HP = 18 nm	4.205 nm
EUV line/space	49.5	HP = 15 nm	4.885 nm

The LER values listed in Table S6 were extracted from representative SEM images obtained under different exposure sessions and sample histories. Therefore, these values should be used to evaluate representative image quality under each exposure condition rather than to establish a universal half-pitch-dependent LER trend.

SEM Image Selection and LER Analysis

All SEM images used for quantitative LER analysis were processed using the same image-analysis workflow. Regions affected by apparent SEM imaging artifacts, drift, vibration, charging, or field distortion were excluded from quantitative edge extraction. Ultrafine features with insufficient SEM contrast were used only as limiting-resolution demonstrations and were not used for LER extraction.

Just Accepted